Journal of Materials Chemistry C

Accepted Manuscript

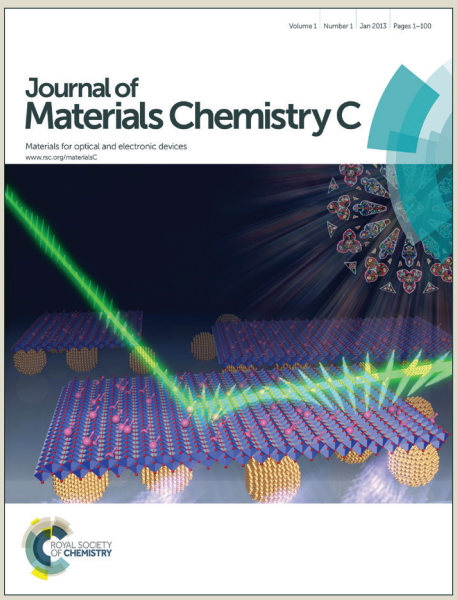

ROYAL SOCIETY OF CHEMISTRY

www.rsc.org/materialsC

Journal Name

RSCPublishing

ARTICLE

A prototypical development of plasmonic multiferroic bismuth ferrite particulate and fiber nanostructures and their remarkable photocatalytic activity under sunlight

Cite this: DOI: 10.1039/x0xx00000x

Received 00th April 2014,
Accepted 00th JApril 2014

DOI: 10.1039/x0xx00000x

www.rsc.org/

Sakar Mohan[a], Balakumar Subramanian[a,*] and Ganesamoorthy Sarveswaran[b]

We have developed a unique plasmonic multiferroic photocatalyst by integrating silver nanoparticles (Ag NPs) with the multiferroic bismuth ferrite ($BiFeO_3$-BFO) particulate and fiber nanostructures and showed a remarkable photocatalytic enhancement under the direct exposure of sunlight. Sol–gel and electrospinning methods were employed to fabricate these nanostructures and a modified chemical reduction method was formulated to decorate Ag NPs for effective plasmon sensitization process. The observed red shift and wide optical absorption profile of plasmonic BFO nanostructures promised for an enhanced absorption in visible light region. The photocatalytic activity of these nanostructures was studied on the degradation of methylene blue (MB) under the irradiation of direct sunlight. Ag NPs-decorated BFO particulates and fibers significantly shortened the photocatalytic degradation by 2 h as compared to their parent BFO nanostructures. The observed phenomenon was attributed to a synergistic effect, wherein the localized surface plasmon resonance (LSPR) of Ag NPs augmented the sunlight absorption as well as trapped the excited carriers. Thereby, these sensitized Ag NPs facilitated the promotion of the charge carriers to the catalyst–dye interface leading to a rapid generation of redox species that increased the degradation rate under the sunlight irradiation.

1. Introduction

The process of photocatalysis involves the absorption of photons to produce dynamic electrons and holes to initiate the oxidation/reduction of the molecules[1]. This is recognized to be more useful for a wide range of applications such as water splitting, waste water treatment, disinfections, CO_2 diminution, and self-cleaning surfaces.[2] In spite of a significant growth in this field, there has been a shortfall in the development of efficient photocatalyst for industrial applications. This inability is owing to the lower photocatalytic efficiency and lack of visible light responsiveness of photocatalytic materials.[3] In a single-phase photocatalyst, the migration of the charge carriers is random and thus the excited carriers have higher possibilities to recombine, causing low photocatalytic efficiency.[4] Even though materials like ZnO and TiO_2 show enhanced photocatalytic activity, they work under the irradiation of UV light and it entails the use of customized UV light sources that are likely impractical in the current scenario of energy consumption. Hence, utilizing sunlight in the field of photocatalysis has generated significant quantum of research in developing visible light-driven photocatalysts.

Bismuth ferrite, $BiFeO_3$ (BFO) is a well-known multiferroic material that shows spontaneous magnetic and ferroelectric properties at room temperature and has also been recognized as a visible light-driven photocatalyst due to its narrow band gap (~2.2 eV). The coupling between various ferroic properties in BFO, offers multi degrees of freedom for manipulating their photocatalytic activities.[5] Due to these advantages, BFO assumes significance as a prototypical material for next generation, solar-based energy material.[6] Eventually, customizing its ferroic properties, for the intended applications, is of prime importance and this can be achieved by manipulating BFO at nanoscale.

In contrast, enhanced photocatalytic activity has been demonstrated in the multi-component systems and it is realized that they can show synergistic photocatalytic efficiency in comparison to their single component state.[7-9] One such multi-component approach entails metalizing the photocatalysts with nanoscale noble metals such as Au, Ag, and Pt, known as plasmon sensitization.[10] These plasmon sensitizers activate the photocatalysts in two distinct ways, known as Schottky junction and localized surface plasmon resonance (LSPR).[11] The most

competent feature of plasmonic photocatalyst is the LSPR, which refers to the resonant condition between the oscillating electrons of metal and the incident light. LSPR offers several advantages to the photocatalyst that mainly includes, (1) tuning the photocatalyst to be more receptive to the visible light,[12] (2) acts as charge carrier trappers where it significantly reduces the recombination,[13] (3) facilitates the excitation of more number of charge carriers by the local electric field created by LSPR,[14] (4) it enhances the redox reaction by heating up the surrounding environment,[15] and (5) it polarizes the molecules for better adsorption on the photocatalyst and leads to an efficient degradation process.[16]

Nevertheless, in addition to the plasmon sensitizations, improving the photocatalytic efficiency also requires a rational design on the morphologies and dimensions of the photocatalyst.[17] In contrast to other nanostructures, the one-dimensional (1D) nanostructures show enhanced structural, physical, and chemical properties as a result of their confined and unconfined dimensions.[18] The confined dimension can discretely transmit the energy (due to electrons, photon, and phonon), while the unconfined dimension can transmit it collectively.[19] The former are known as nano-phenomena and the latter are known as bulk phenomena. The key and foremost concept in the photocatalytic process is the separation of photo-induced charge carriers and this can be improved by increasing delocalization of electrons which is a typical phenomenon occurring in the 1-D nanostructures.[20] It is therefore expected that this dimension-dependent photocatalytic process can be clearly distinguished in the case of 1-D materials while comparing to the particulate systems.

In this perspective, we present here our interesting results on the fabrication of pure and silver plasmon-sensitized bismuth ferrite particulate and fiber nanostructures fabricated by sol–gel and electrospinning methods, respectively. A modified chemical reduction method was developed to reduce Ag NPs and decorate them on the surface of these BFO nanostructures. A rational photocatalytic enhancement was observed in the Ag-sensitized BFO while the dimension-dependent photocatalytic activity was also observed in the case of undecorated BFO particulate and fiber systems.

2. Experimental

2.1. Synthesis of nanostructured BFO particulates

The nanostructured particulates of BFO were synthesized by sol–gel process as reported in our recent report.[21] In the typical process, the metal nitrates of bismuth ($Bi(NO_3)_3\ 5H_2O$) and iron ($Fe(NO_3)_3\ 9H_2O$) precursors were taken in 1:1 molar ratio (0.1 M) and dissolved in 30 ml of de-ionized water containing 2 ml of 70%-concentrated nitric acid (HNO_3). To this, 10 ml of 0.1 M citric acid was added for gelling purposes and stirred well to obtain a homogeneous mixture. Then the sol was heated up to ~80^oC to obtain gel and dried to powder. Finally, the end-powder was annealed at 550^oC for 2 h to obtain the BFO phase particulates.

2.2. Synthesis of nanostructured BFO fibers

BFO nanofibers were also fabricated by electrospinning method as described in our previous report.[22] In the typical procedure, the ($Bi(NO_3)_3\ 5H_2O$) and ($Fe(NO_3)_3\ 9H_2O$) were taken in the proportionate molar ratio of 1:1 (0.8 mol) and dissolved in 10 ml of solution containing glacial acetic acid ($C_2H_4O_2$) and de-ionized water. To this 1 g of polyvinyl pyrrolidone (PVP - M.W. 13, 00, 000) was added and stirred for 6 h to get a homogenous precursor for the electrospinning process. The obtained solution was loaded in a plastic syringe equipped with a stainless steel needle and connected to a high voltage of 15 kV. The flow rate of the solution was set as 0.2 ml/h and the aluminum foil spread-fiber collector was kept at a distance of 12 cm from the needle. Subsequently, the electrospun BFO/PVP fibers were collected and annealed at 550^oC for 2 h to obtain BFO phase nanofibers.

2.3. Sensitization of Ag NPs on BFO nanostructures

A modified chemical reduction method was developed to form and decorate Ag NPs on the surface of BFO particulates and fibers. In this process, 0.1 M and 1 wt% of the fabricated BFO and silver nitrate ($AgNO_3$) precursor were taken, respectively, in 50 ml solution containing de-ionized water–ethanol in 1:4 ratios. This entire solution was then dispersed/ dissolved with the help of a sonicator to obtain a homogenous mixture. Then a freshly prepared 100 ml of 0.1 M of sodium borohydride ($NaBH_4$) was dripped into the above solution kept in an ice-bath under continuous mechanical stirring. The subsequent color change from brown to dark-brown confirmed the formation and decoration of Ag NPs on BFO. The final solution was then dried at 80^oC to obtain the Ag NPs-decorated BFO particulate and fiber powders.

2.4. Photocatalytic experiment

Before starting the ideal experiment, a series of trial experiments (results have not shown here) were carried out in order to optimize the amount of photocatalyst in the photocatalytic experiments. This optimization was essentially carried out based on two factors, (1) to obtain an optimal amount of photocatalyst which should not get turbid in the dye medium (turbidity of the photocatalyst would limit the light penetration and scattering of the light), and (2) to achieve a minimum amount of photocatalyst to degrade the given amount of dye in an effective period of time. Accordingly, the trial experiments were carried out by choosing various amount of photocatalyst, such as 1, 3, 5, 6, 8 mg. In these trials the slight increment of photocatalyst from 5 to 6 mg led to considerable changes in the photocatalytic process. This concentration (6 mg) was found to be the initial concentration to initiate the turbidity like formation in the dye medium, and it also intervened in the absorption spectra which led to the appearance of an overlapped graphs. Eventually, the degradation graphs were also found to be ambiguous. Therefore 5 mg of photocatalyst in the given volume of dye solution is

considered to be an optimum concentration for further photocatalytic experiments.

3. Results and discussion

3.1. Crystal structure and phase analysis

The crystal structure of the fabricated pure and Ag-decorated BFO particulates (Ag:BFO-P) and fibers (Ag:BFO-F) were analyzed by powder X-ray diffraction (XRD) technique and the results are shown in Fig. 1. The XRD pattern reveals the diffraction peaks corresponding to phase BFO as well as metallic Ag. It is found that the BFO and Ag possess rhombohedral (R3c space group) (JCPDS card no. 20-0169) and face-centered cubic structure (fm3m space group) (JCPDS card no. 89-3722), respectively.

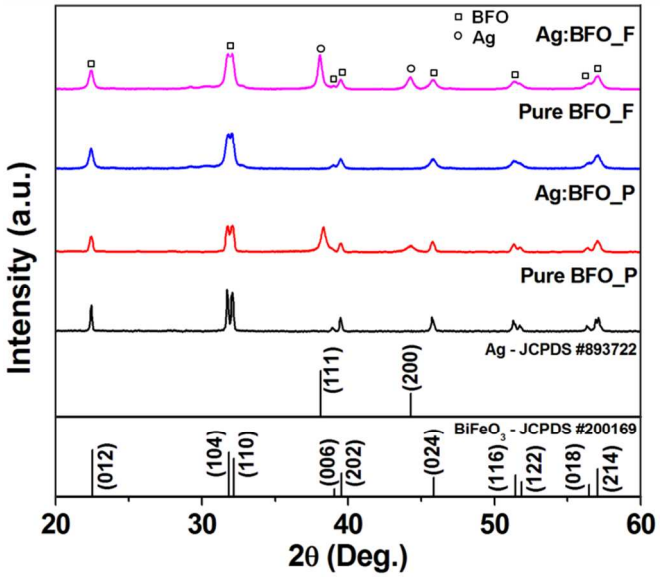

Fig. 1 XRD pattern of pure and Ag nanoparticles-decorated BFO particulate and fiber nanostructures.

It is noteworthy that no shift in the doublet peak of Ag:BFO-P and Ag:BFO-F is observed with respect to the doublet peak of corresponding undecorated BFO. This indicates that the integration of Ag is only on the surface or at grain boundary and not into the lattice or interstitial sites of host BFO.[23] Further, the decorated Ag nanoparticles were in metallic state and not as silver oxide, which can be corroborated with its JCPDS data that correspond to the metallic Ag as shown in Fig. 1.

3.2. Morphology analysis and mechanics of Ag decoration

Figure 2(a–h) shows the field emission scanning electron micrographs of the pure and Ag-decorated particulates and fibers of BFO.

The size of the synthesized BFO particles is found to be 150 nm. On the other hand, the diameter and length of nanofibers is found to be 90 nm and a few micrometers, respectively. These size parameters of both particles and fibers remained unaffected even after the Ag decoration. The average particle size of the decorated Ag is found to be around 20–30 nm, although as large as 55 nm were also present. Figure 3(a–h) shows the high resolution transmission electron micrographs of the obtained BFO nanostructures. The obtained nanofibers were composed of dense nanocrystalline grains with size around 35 nm.

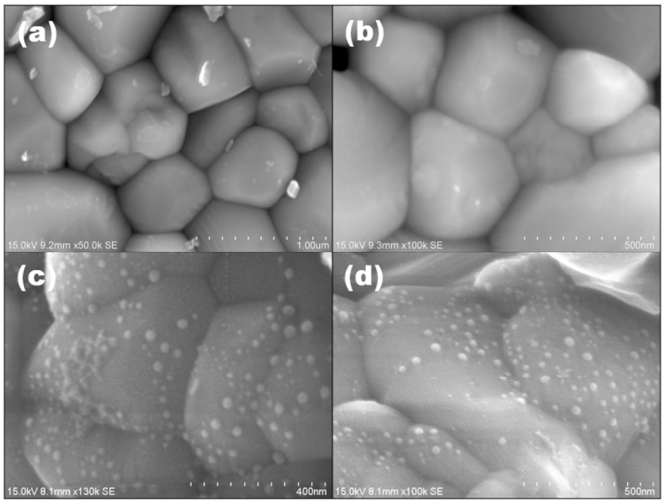

Fig. 2 (a–d) FESEM micrographs of (a, b) pure BFO and (c, d) Ag NPs-decorated BFO particulates.

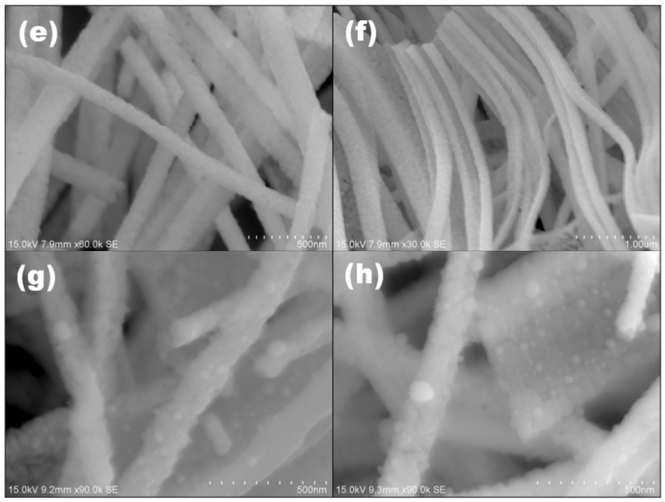

Fig. 2 (e–h) FESEM micrographs of (e, f) bare BFO and (g, h) Ag NPs-decorated BFO fibers.

The mechanism for the formation and deposition of Ag NPs on the surface of BFO nanostructures is illustrated in Fig. 4 and proposed as follows. The presence of ethanol in the solution makes it polar and the negatively charged OH^- groups form on the surface of BFO. This behaves like anchoring sites for the positively charged Ag ions (Ag^+). With the addition of the reducing agent ($NaBH_4$), these electro-statically bound Ag^+ ions get further reduced and the subsequent crystallization process ensures the formation and deposition of Ag NPs onto these nucleation sites and decorates the host BFO nanostructures.[24]

3.3. Optical properties

A remarkable optical enhancement is observed in the Ag-decorated BFO nanostructures in comparison to the undecorated BFO as shown in Fig. 5(a).

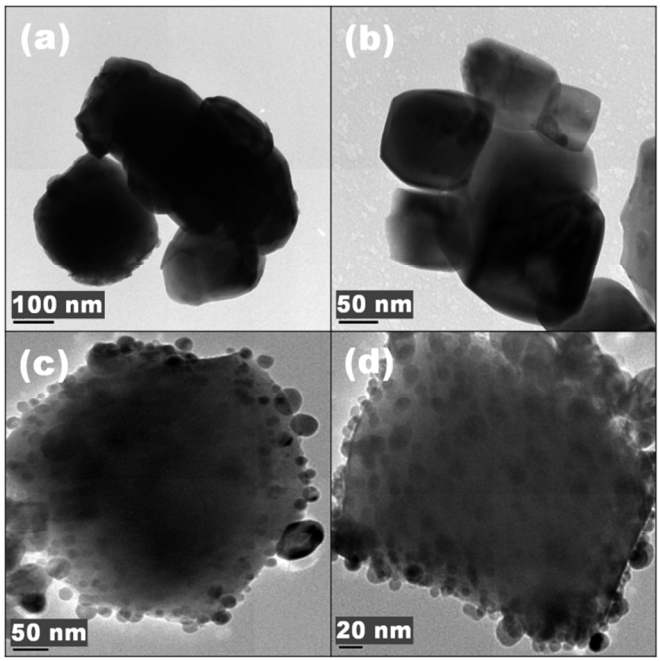

Fig. 3 (a–d) HRTEM micrographs of (a, b) pure BFO and (c, d) Ag NPs-decorated BFO particulates.

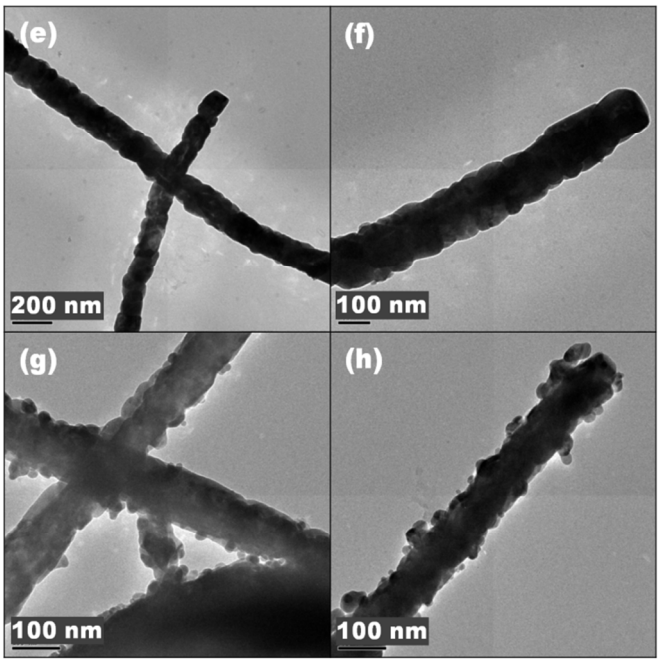

Fig. 3 (e–h) HRTEM micrographs of (e, f) pure BFO, (g, h) Ag NPs-decorated BFO fibers.

It is evident from the absorption profile that the decorated Ag has notably red shifted and widened the typical optical absorption profile of BFO nanostructures. This can be attributed to the formation of plasmon-induced bands due to the overlapping of the absorption bands of plasmonic Ag and BFO nanostructures.

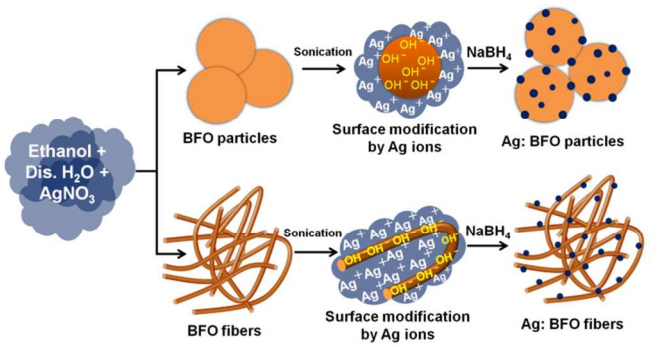

Fig. 4 Formation and decoration mechanism of Ag NPs on the surface of BFO particulate and fiber nanostructures.

The surface plasmon (oscillating electrons) of the coupled Ag NPs establishes a dipole interaction with the time varying electric field of the incident light. Intense oscillation of these surface electrons leads to a stronger absorption of visible light[25] as illustrated in Fig. 5(b). Further, the decorated Ag nanoparticles make the BFO as a charge polarized surface, which lengthens the propagation of light thereby leading to an improved light trapping in these nanostructures. This phenomenon could be attributed to the observed broad absorption peak.[26,27] Thus, the BFO nanostructures in the vicinity of Ag nanoparticles showed an enhanced optical absorption in the visible region.

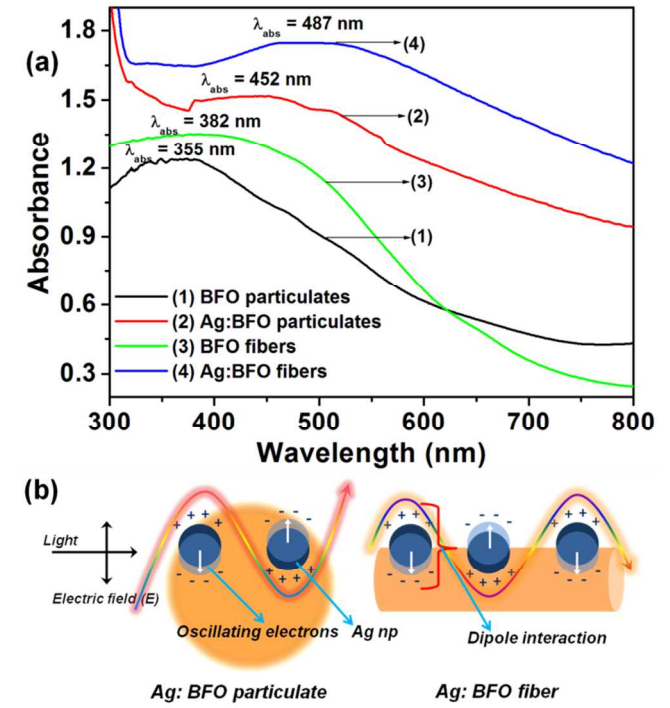

Fig. 5 (a) UV-visible absorption profile of pure and Ag plasmon-sensitized BFO particulate and fiber nanostructures (b) depiction of light absorption in the plasmon-sensitized BFO nanostructures.

The band gap energy of the BFO particulate and fiber is 2.3 eV and 2.4 eV, respectively, as deduced from the UV-visible diffuse reflectance curves (Fig. 6(a)) by applying Kubelka-Munk (KM) function[28] as shown in the insert of Fig. 6(a).

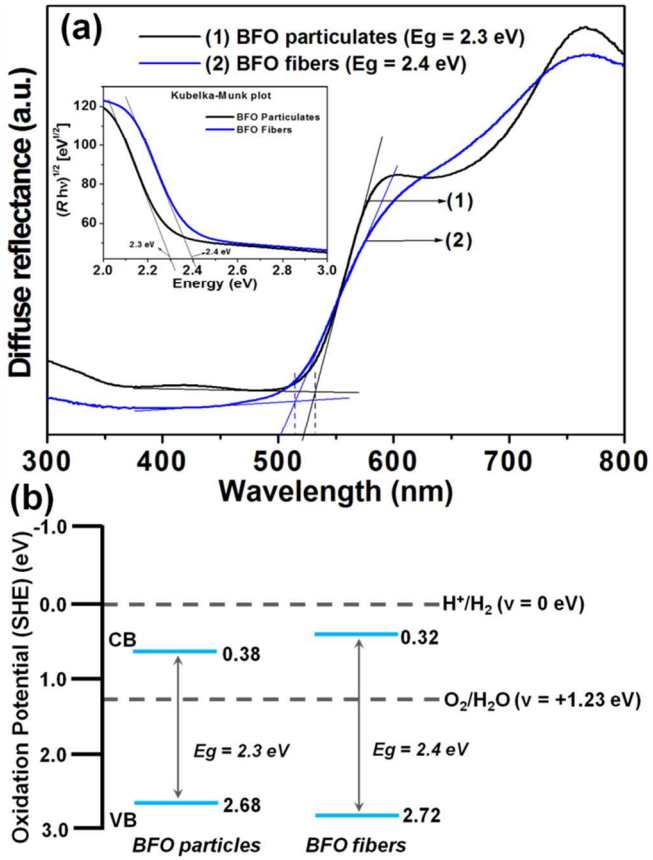

Fig. 6 (a) UV-visible diffuse reflectance spectrum for band gap determination, (insert: Kubelka-Munk plot) and, (b) Calculated band edge (VB, CB) position of BFO particulate and fiber nanostructures.

From the obtained band gap energy, the location of valence band (VB) and conduction band (CB) in particulate and fiber system is calculated. Accordingly, the CB and VB potentials of BFO can be determined by using the empirical equation:[28,29] $E_{VB} = X - E^e + 0.5\ E_g$, where E_{VB} is the VB edge potential, X is the electronegativity of the semiconductor, which is the arithmetic mean of electronegativity of constituent atoms and first ionization energy. E^e is the energy of free electrons on the hydrogen scale (~4.5 eV) and E_g is the band gap energy of the semiconductor. Similarly, E_{CB} can be determined from the equation $E_{CB} = E_{VB} - E_g$ The determined band edge position of BFO particulate and fiber and their comparison with potential of standard hydrogen electrode (SHE) is depicted in Fig. 6(b).

3.4. Photocatalytic studies

The photocatalytic activity of the fabricated pure and Ag-decorated BFO nanostructures were studied on the degradation of methylene blue (MB) organic dye under the direct sunlight irradiation. From the optimization process as discussed in the section 2.4., in the typical experiment, 5 mg of photocatalyst was taken in 100 ml of MB solution from the stock of 10 mg/l for the photocatalytic experiment. Prior to the sunlight exposure, the dye-photocatalyst mixture was stirred well by using a magnetic stir in a dark condition to let the solution attain adsorption-desorption equilibrium between the photocatalyst and dye. This experiment was also carried out for different period of time and 30 min found to be an optimum period to reach equilibrium condition. Then the subsequent sunlight driven degradation of MB was recorded periodically by using UV-visible absorption spectrometer. The obtained degradation and C/C_0 ratio graphs are shown in Fig. 7(a–f).

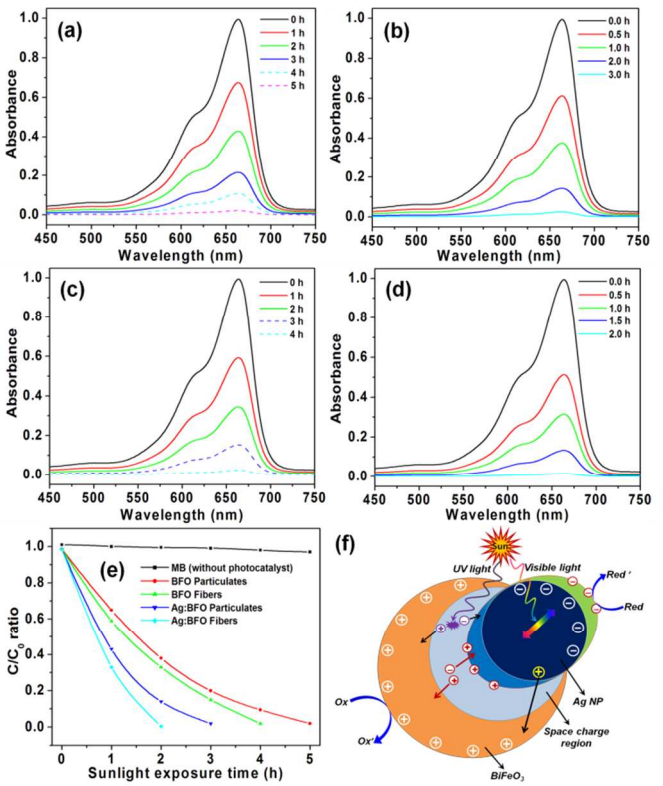

Fig. 7 Photocatalytic degradation of MB dye by the particulates of (a) pure BFO (b) Ag NPs-decorated BFO and the fibers of (c) pure BFO (d) Ag NPs-decorated BFO, (e) C/C_0 graph, and (f) general photocatalytic process in Ag-sensitized BFO.

In a span of 3 h, Ag:BFO-P degraded almost the entire dye, while it was only 68% in the case of pure BFO particles and another 2 h were required for them to achieve the same amount of degradation as achieved by Ag:BFO-P (shown as dotted lined graphs in Fig. 7(a)). Alternatively, the Ag: BFO-F required only 2 h to degrade the entire dye. Pure BFO nanofibers degraded only 58% and it required another span of 2 h to achieve nearly the same degradation percentage as obtained in the case of Ag:BFO-F (shown as dotted lined graphs in Fig. 7(c)). The general photocatalytic phenomenon in a plasmonic photocatalyst[30] is depicted in Fig. 7(f).

The observed photocatalytic activity of these nanostructures can be investigated in two perspectives. One is the dimension-dependent and another is the plasmon-induced photocatalytic activity of these BFO particle and fiber systems.

The photocatalytic enhancement in the 1-D fibers of BFO could be readily attributed to its confinement-induced features. The lateral structure of these 1-D materials essentially decreases the recombination possibilities of photo-induced charge carries due to the enhanced delocalization of electrons[20,31] as depicted in Fig. 8. As it can be seen in the micrographs (Figs. 2(e-h) and 3(3-h)) the nanofibers of BFO are likely made up of closely packed crystallites that are stacked one dimensionally. In such a system, once the charge separation is established, the electrons excited to the CB get delocalized and diffuse into these inter-connected crystallites and reduce the probability of charge recombinations.[32] In this circumstance, the energy applied for the charge separation is sustained in the system that is utilized for the production of redox species in the medium that degrades the dye molecules very effectively.

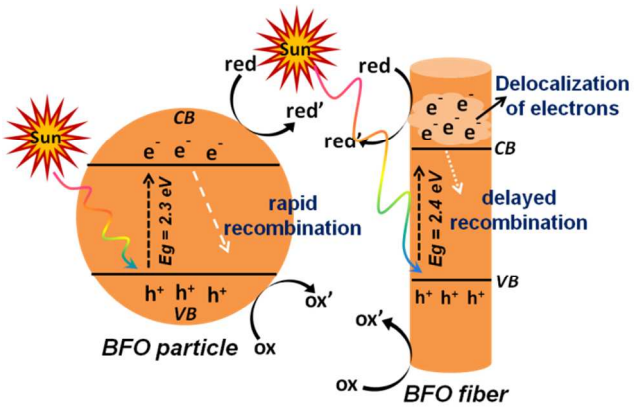

Fig. 8 Concept of dimension-dependent photocatalytic efficiency in BFO particulate and fiber systems.

Similarly, the mechanism of the observed photocatalytic efficiency in Ag-decorated BFO nanostructures can be attributed to its surface plasmon-induced rapid redox processes under the irradiation of sunlight. The surface plasmon resonance (SPR) of nanoscale noble metals refers to the process in which the electrons in the CB of the plasmonic metal undergo a collective oscillation induced by the time varying electrical field of the impinging photons,[33] and subsequently these oscillating charges likely increase the electrical polarization in the near surface of the photocatalyst.[34] Accordingly, the electrical polarization induced by the SPR of Ag nanoparticles causes a large local electrical field enhancement in BFO which leads to a stronger visible light absorption in these Ag:BFO hybrid nanostructures. As a result, more number of charge carriers (e^-/h^+ pairs) generated in BFO and the subsequent injection of the excited electrons into the CB of Ag effectively reduces the recombination probabilities via the trapping of these electrons in the CB and enhances the charge separation in BFO.[30,35]

Accordingly, these separated electrons and holes migrate to the surface of Ag:BFO catalyst and involve in redox reactions with sorbed species.[36] Specifically, the holes (h^+) in the valance band (VB) may react with surface-bound H_2O or OH^- to produce the hydroxyl radical and the electrons (e^-) in the conduction band (CB) are picked up by oxygen to generate superoxide radical anion ($O_2^{\bullet-}$), as given in the following equations (1)-(3).

Absorption of photons by the photocatalyst (PC)

$$PC + h\nu \rightarrow e^-_{cb} + h^+_{vb} \quad (1)$$

formation of superoxide radical anion

$$O_2 + e^-_{cb} \rightarrow O_2^{\bullet-} \quad (2)$$

neutralization of OH^- group into $^\bullet OH$ by the hole

$$(H_2O \Leftrightarrow H^+ + OH^-)_{ads} + h^+_{vb} \rightarrow {}^\bullet OH + H^+ \quad (3)$$

As mentioned that in the photocatalytic process, the hydroxyl radical ($^\bullet OH$) and superoxide radical anions ($O_2^{\bullet-}$) are the primary oxidizing species and they would further degrade the pollutants as shown in the following equations (4)-(5).

oxidation of the organic pollutants via successive attack by $^\bullet OH$ radicals

$$R + {}^\bullet OH \rightarrow R'^\bullet + H_2O \quad (4)$$

or by direct reaction with holes

$$R + h^+_{vb} \rightarrow R^{\bullet+} \rightarrow \text{degradation products} \quad (5)$$

In the photocatalytic mechanism, we propose that the electrons are transferred from the BFO to Ag via band-bending phenomenon that typically occurs in the semiconductors when they contact with another phase such as liquid, molecules, metals, etc.[37] We also propose that the bands in BFO would bend downwards when they establish the contact with Ag due to the thermal equilibration of its Fermi level energy.[30] Fig. 9 shows the band energy level of BFO (based on the electron affinity and band gap energy) and the Work function of Ag metal in an ideal condition before the contact is established.[38]

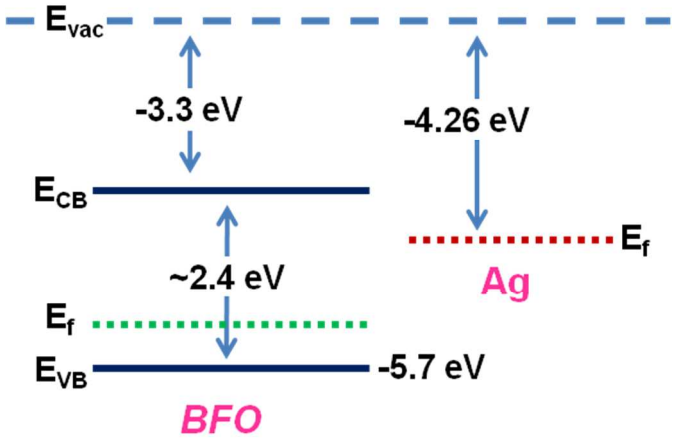

Fig. 9 Band energy level of BFO (electron affinity and band gap energy) and the Work function of the Ag metal before their contact.

We suggest the downward band bending in BFO in the vicinity of Ag metal NPs is because of the following reasons.[30] In general the band bending phenomenon is associated with the conducting *type* (*n/p*) of the semiconductors. Further, it is also dependent upon the Fermi energy level (E_f), work function (W) and redox potential (E_{redox}) of the semiconductor, sensitizing metal and the potential required for redox reaction to take place, respectively. Accordingly, for a *p–type* semiconductor,

before its contact to the metal and solution, if their energy parameters satisfy $E_f < W < E_{redox}$, then their bands will tend to bend downwards after the contact is established with the metal as shown in Fig. 10(a)-(b). Similarly, for an *n–type* semiconductor, before its contact to the metal and solution, if their energy parameters satisfy $E_f > E_{redox} > W$, then their bands will tend to bend upwards after the contact is established.[30]

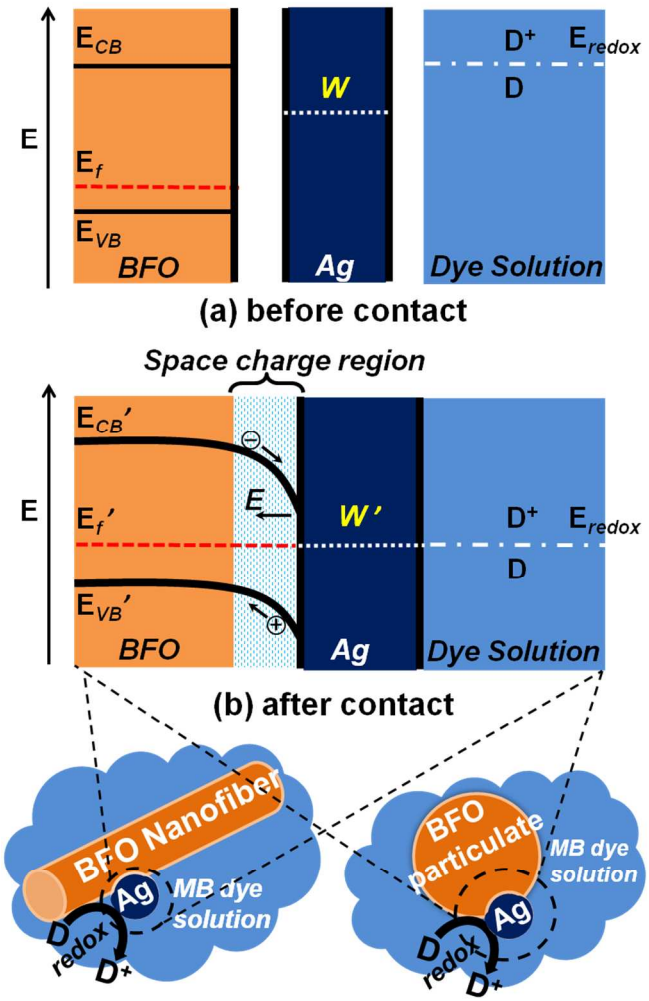

Fig. 10 Mechanism of photo-induced carrier transport and band bending in the Ag plasmon-sensitized BFO particulate and fiber system, (a) before contact and (b) after contact of BFO with Ag

It is known that the BFO is a p-type semiconductor,[39] and from the band energy structure as shown in Fig. 9(a)-(b), the Fermi level energy of BFO can be lied below the work function of Ag (-4.26 eV) and the redox potential, which satisfies the $E_f < W < E_{redox}$ condition. Therefore, once the contact is established between the Ag, BFO and dye medium, the bands in BFO bends downwards and facilitates the transfer of electrons from the CB of BFO to Ag NPs as shown in Fig. 10(b). Thus the transfer of electrons from the BFO to Ag is thermodynamically supportive[40] and leads to the effective recombination delay that eventually resulting to the enhanced photocatalytic activities in these plasmon sensitized BFO particulate and fiber nanostructures compared to the bare BFO.

4. Summary and conclusion

To summarize, bismuth ferrite particulates and fibers nanostructures were fabricated by sol-gel and electrospinning methods, respectively. These fabricated nanostructures were further decorated with silver nanoparticles through a chemical reduction process and studied for their photocatalytic degradation of MB dye under the irradiation of direct sunlight. The observed degradation characteristics of particulate and fiber systems were attributed to their dimension-dependent recombination delay which was occurred as a result of an enhanced delocalization of electrons in the CB of BFO fibers compared to particulates. As a result, while the BFO fibers degraded the entire dye in a span of 4 h, the particulates took 5 h to degrade the same amount of dye. On the other hand, the degradation efficiency of Ag:BFO nanostructures was found to be very rapid as compared to undecorated BFO. Accordingly, the Ag:BFO particulate and fiber nanostructures advanced the degradation process by 2 h where they took only 3 and 2 h respectively, to degrade the entire dye. The observed photocatalytic enhancements in these Ag:BFO nanostructures were attributed to the plasmon-driven photocatalytic process, where more number of electrons was excited to the CB of BFO through the stronger absorption of visible light due to the surface plasmons of Ag nanoparticles. Further, as these excited electrons were effectively injected and trapped into the CB of Ag via the band bending phenomenon, it significantly reduced the carrier recombination in these Ag sensitized BFO nanostructures. Thereby, the sustained energy in the system promoted the trapped charge carriers to the dye–photocatalyst interface and led to an effective degradation of dye through the production of active redox species. In conclusion, developing such unique plasmon-sensitized stable oxide semiconductor photocatalysts with lower band gap shows a promising future for solar energy-driven environmental applications, as one of them reported here.

Acknowledgements

Authors gratefully acknowledge the Council of Scientific and Industrial Research (CSIR), Govt. of India for funding to carry out this research project.

Notes and references

[a,*]National Centre for Nanoscience and Nanotechnology, University of Madras, Guindy campus, Chennai 600025, India. Fax: 044-22352494/ 22353309; Tel: 044-22202749, *E-mail: balasuga@yahoo.com.
[b]Materials Science Group, Indira Gandhi Centre for Atomic Research, Kalpakkam 603102, India.

1. K. Hashimoto, H. Irie and A. Fujishima, *Jpn. J. Appl. Phys.*, 2005, **44**, 8269.
2. (a) M. R. Hoffmann, S. T. Martin, W. Choi and D. W. Bahnemannt, *Chem. Rev.*, 1995, **95**, 69; (b) J. M. Herrmann, *Catal. Today*, 1999, **53**, 115.

3. P. Wang, B. Huang, Y. Dai and M. H. Whangbo, *Phys. Chem. Chem. Phys.*, 2012, **14**, 9813.
4. Thang Cao Dinh, Minh Hao Pham, Yongbeom Seo, Freddy Kleitz and Trong On Do, *Nanoscale*, 2014, DOI: 10.1039/C3NR06602A
5. Carlos Antonio Fernandes Vaz, Urs Staub, *J. Mate. Chem. C,* 2013, **1**, 6731-42
6. A. I. Hochbaum, P. Yang, *Chemical Reviews*, 2009, **110**, 527.
7. Y. F. Fang, W. H. Ma, Y. P. Huang, C. W. Cheng, *Chem. Eur. J.,* 2013, **19**, 3224.
8. Jun Seop Lee, Jyongsik Jang, *Journal of Industrial and Engineering Chemistry*, 2014, **20**, 363.
9. Zahed Shami and Naser Sharifi-Sanjani, *CrystEngComm*, 2014, **16**, 910.
10. Manda Xiao, Ruibin Jiang, Feng Wang, Caihong Fang, Jianfang Wang and Jimmy C. Yu, *J. Mater. Chem. A*, 2013, **1**, 5790
11. Z. Wang, J. Liu and W. Chen W, *Dalton Trans.* 2012, **41**, 4866; R. B. M. Schasfoort and A. J. Tudos (ed) *Handbook of Surface Plasmon Resonance (Cambridge: RSC publishing)*, 2008.
12. I. Thomann, B.A. Pinaud, Z. Chen Z, B. M. Clemens, T. F. Jaramillo and M. L Brongersma, *Nano Lett.* 2011, **11** 3440.
13. S. Mubeen, G. Hernandez-Sosa, D. Moses, J. Lee and M. Moskovits, *Nano Lett.*, 2011, **11** 5548.
14. C. Langhammer, Z. Yuan, I. Zoric and B. Kasemo, *Nano Lett.*, 2006, **6**, 833.
15. Z. C. Wu, Y. Zhang, T. X. Tao, L. Zhang and H. Fong, *Appl. Surf. Sci.,* 2010, **257**, 1092.
16. S. Sun, W. Wang, L. Zhang, M. Shang and L. Wang, *Catal. Commun.*, 2009, **11**, 290.
17. (a) Haolan Xu, Wenzhong Wang, and Wei Zhu, *J. Phys. Chem. B*, 2006, **110**, 13829; (b) Giuseppe Cernuto, Norberto Masciocchi, Antonio Cervellino, Gian Maria Colonna and Antonietta Guagliardi, *J. Am. Chem. Soc.* 2011, **133**, 3114.
18. A. I. Hochbaum, P. Yang, *Chemical Reviews*, 2009, **110**, 527.
19. S. D. Rupesh, A. P. Ranjit, Jin-Han Lin, Yuan-Ron Ma, *Adv. Func. Mate.,* 2012, **22**, 3326.
20. H. J. Yun, H. Lee, J. B. Joo, W. Kim and J. Yi, *J. Phys. Chem. C,* 2009, **113**, 3050.
21. Sakar Mohan, Balakumar Subramanian, Indranil Bhaumik, Pradeep Kumar Gupta and N. Sellamuthu Jaisankar, *RSC Adv.*, 2014, **4**, 16871
22. Sakar Mohan, Balakumar Subramanian, *RSC Adv.,* 2013, **3**, 23737.
23. Yongchun Lu, Yanhong Lin, Dejun Wang, Lingling Wang, Tengfeng Xie, Tengfei Jiang, *Journal of Physics D:Applied Physics*, 2011, **44**, 315502.
24. Ren Der Jean, Kuo Chuang Chiu, Tsung Han Chen, Chun Hua Chen, and Dean Mo Liu, *J. Phys. Chem. C*, 2010, **114**, 15633.
25. (a) Peng Wang, Baibiao Huang, Ying Daia, Myung-Hwan Whangbo, *Phy. Chem. Chem. Phy.,* 2012, **14**, 9813; (b) Matthew J. Kale, Talin Avanesian and Phillip Christopher, *ACS Catal.* 2014, **4**, 116.
26. (a) Koichi Awazu, Makoto Fujimaki, Carsten Rockstuhl, Junji Tominaga, Hirotaka Murakami, Yoshimichi Ohki, Naoya Yoshida and Toshiya Watanabe, *J. Am. Chem. Soc.,* 2008, **130**, 1676; (b) Hairen Tan, Rudi Santbergen, Arno H. M. Smets and Miro Zeman, *Nano Lett.*, 2012, **12**, 4070.
27. (a) S. L. Smithaa, K. M. Nissamudeena, Daizy Philipb, K. G. Gopchandran, *Spectrochimica Acta Part A,* 2008, **71**, 186; (b) Li Jin, Kun Qian, Zhiquan Jiang, Weixin Huang, *Journal of Molecular Catalysis A:Chemical*, 2007, **274**, 95.
28. (a) A.B. Murphy, *Solar Energy Materials & Solar Cells*, 2007, 91, 1326; (b) P. Kubelka, *J. Opt. Soc. Am.*, 1948, 38, 448; (c) P. Kubelka, F. Munk, *Z. Tech. Phys.,* 1931, 12, 593
29. (a)Shun Li, Yuan Hua Lin, Bo Ping Zhang, Jing Feng Li, and Ce Wen Nan, J. App.Phy., 2009, **105**, 054310. (b) A. H. Nethercot, *Phys. Rev. Lett.*, 1974, **33**, 1088; (c) Y. Kim, S. J. Atherton, E. S. Brigham and T. E. Mallouk, *J. Phys. Chem.,* 1993, **97**, 11802.
30. Xuming Zhang, Yu Lim Chen, Ru-Shi Liu and Din Ping Tsai, *Rep. Prog. Phys.*, 2013, **76**, 046401.
31. T. Freddy Rabouw, Per Lunnemann, J. A. Relinde van Dijk Moes, Martin Frimmer, Francesca Pietra, A. Femius Koenderink, and Daniel Vanmaekelbergh, *Nano Lett.,* 2013, **13**, 4884.
32. (a) Helin Huang, Dustin E. Gross, Xiaomei Yang, Jeffrey S. Moore, and Ling Zang, *ACS Appl. Mater. Interfaces*, 2013, **5**, 7704; (b) Mustafa Supur, Yusuke Yamada, Mohamed E. El-Khouly, Tatsuhiko Honda and Shunichi Fukuzumi, *J. Phys. Chem. C*, 2011, **115**, 15040.
33. K. Scott Cushing, Jiangtian Li, Fanke Meng, R. Tess Senty, Savan Suri, Mingjia Zhi, Ming Li, D. Alan Bristow and Nianqiang Wu, *J. Am. Chem. Soc.*, 2012, **134**, 15033.
34. (a) Zhi Wei Seh, Shuhua Liu, Michelle Low, Shuang-Yuan Zhang, Zhaolin Liu, Adnen Mlayah, and Ming-Yong Han, *Adv. Mater.,* 2012, **24**, 2310; (b) B. David Ingram and Suljo Linic, *J. Am. Chem. Soc.*, 2011, **133**, 5202.
35. L. J. Di, H. Yang, G. Hu, T. Xian, J. Y. Ma, J. L. Jiang, R. S. Li, Z. Q. Wei, *J Mater Sci: Mater Electron*., 2014, **25**, 2463.
36. Parmiss Mojir Shaibani, K. Prashanthi, Amirreza Sohrabi and Thomas Thundat, *Journal of Nanotechnology*, 2013, **2013**, Article ID 939531.
37. Amy L. Linsebigler, Guangquan Lu, John T. Yates Jr., *Chem. Rev.*, 1995, **95**, 735.
38. (a) Leonard Loh, Joe Briscoe, Steve Dunn, *Nanoscale*, 2014, **6**, 7072. (b) R. L. Gao, Y. S. Chen, J. R. Sun, Y. G. Zhao, J. B. Li, and B. G. Shen, *Appl. Phys. Lett.,* 2012, **101**, 152901.
39. (a) B. Vengalis, J. Devenson, A. K. Oginskis, R. Butkute, A. Maneikis, A. Steikoniene, L. Dapkus, J. Banys and M. Kinka, Acta Phys. Pol., A, 2008, **113**, 1095. (b) H. Yang, H. M. Luo, H. Wang, I. O. Usov, N. A. Suvorova, M. Jain, D. M. Feldmann, P. C. Dowden, R. F. DePaula and Q. X. Jia, *Appl. Phys. Lett.*, 2008, **92**, 102113. (c) Yiling Zhang, Andrew M. Schultz, Paul A. Salvador and Gregory S. Rohrer, J. Mater. Chem., 2011, **21**, 4168
40. Shun Li, Jianming Zhang, Md Golam Kibria, Zetian Mi, Mohamed Chaker, Dongling Ma, Riad Nechache, Federico Rosei, *Chem. Commun.,* 2013, **49**, 5856.

For table of content entry

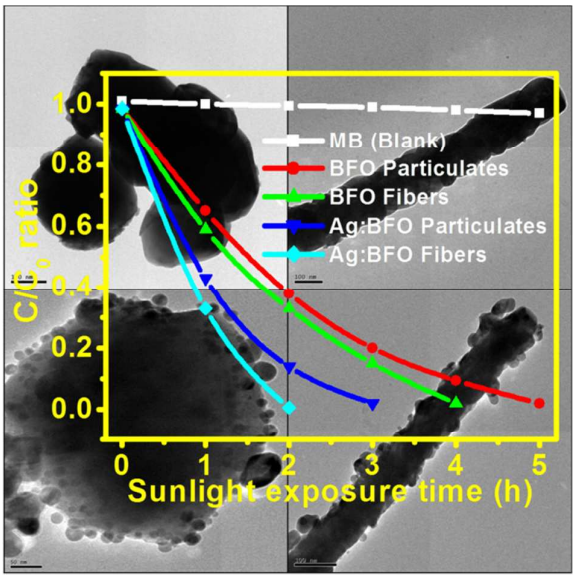

Ag sensitized plasmonic multiferroic $BiFeO_3$ particulate and fiber nanostructures have been developed and demonstrated their sunlight driven photocatalytic degradation.